ARTICLES

Magnetic Properties of 4-nm Cd$_{1-y}$Mn$_y$S Nanoparticles Differing by Their Compositions, *y*

N. Feltin, L. Levy, D. Ingert, and M. P. Pileni*

Laboratoire SRSI, URA CNRS 1662, Universite P et M Curie (Paris VI), BP 52, 4 Place Jussieu, 75231 Paris Cedex 05, France, and CEA−CE Saclay, DRECAM−SCM, 91191 Gif sur Yvette, Cedex, France

In this paper, we present, for the first time, the magnetic properties of Cd$_{1-y}$Mn$_y$S nanocrystals of average size (4 nm) at various compositions, *y*. We demonstrate that the Mn−Mn interactions are markedly enhanced compared to the bulk material. As in the bulk phase, the photoluminescence and the EPR hyperfine structure, both attributed to isolated Mn^{2+} ions in a tetrahedral coordination, behave similarly with increasing composition. At the opposite of the bulk phase, isolated Mn^{2+} ions are observed for a rather large composition (*y* = 0.08) in nanocrystals. We attempt to relate the change of the band gap with composition with the various manganese interactions.

I. Introduction

Diluted magnetic semiconductors (DMS)[1] are alloys in which magnetic ions (Mn^{2+}, Fe^{2+}, Co^{2+}) are diluted in nonmagnetic A^{II}B^{VI} semiconductors (such as CdS, CdTe, ZnSe, ...). DMS bulk materials exhibit a number of interesting magnetooptical effects such a giant Faraday rotation,[2] large Zeeman splitting of carriers,[3] and bound magnetic polarons.[4]

Severals groups[3,4] have showed that exchange interactions, which couple Mn spins antiferromagnetically, have a dominating role in the magnetic properties of DMS's. The theoretical investigations of Larson et al.[5] indicated that superexchange is the main mechanism involved in Mn−Mn exchange interactions with Cd$_{1-y}$Mn$_y$Te and Cd$_{1-y}$Mn$_y$Se. By contrast, for Cd$_{1-y}$Mn$_y$S, the dipolar contribution needs to be taken into account.[6] However, neither of these two models clearly explains the Cd$_{1-y}$Mn$_y$S experimental data.

The presence of localized magnetic ions in a semiconductor alloy leads to exchange interactions between s−p band electrons and the Mn^{2+} d electrons. This sp−d exchange interaction constitutes a unique interplay between semiconductor physics and magnetism. It plays a double role in determining optical properties in that (i) the band gap of the compound is altered depending upon the concentration of the manganese ions and (ii) the 3d levels of transition-metal ions located in the band gap region and d−d transitions dominate the spectrum.

Traces of Mn^{2+} included in II−VI semiconductors result in numbers of isolated Mn^{2+} ions in a tetrahedral coordination which induce luminescence, attributed to energy transfer from the host semiconductor to Mn^{2+} ions in a tetrahedral coordination.[1,7,8]

In the nanometer-size crystallites of semimagnetic semiconductors, many of the physical properties are expected to be influenced by the quantum confinement of the electronic states and, hence, differ from those of the bulk crystals. Due to the quantum dots, the unique properties of these nanostructures have great potential for a variety of applications.

In the nanoscale range, to our knowledge, no magnetic properties of II−VI semiconductors containing Mn^{2+} in their matrixes have been reported. However, some groups have studied their optical properties,[7,9−12] and fluorescence due to isolated Mn^{2+} ions in tetrahedrical coordinations was observed and attributed to a quantum size effect.[7,9−12]

In our previous papers,[13−15] we demonstrated that the size and composition of Cd$_{1-y}$Mn$_y$S nanocrystals can be independently controlled by using reverse micelles as templates. A progressive control of the average size (from 1.8 to 4 nm) and composition (from *y* = 0.03 to 0.3) can be obtained. We demonstrated that the band-gap energy decreases and then increases with increasing composition. The depth of the minimum is more pronounced when the particle size decreases. This is attributed to a marked increase in the interactions between the Mn^{2+} d electrons and the valence and conduction band electrons. Furthermore, the Mn^{2+} photoluminescence observed in the nanocrystals is due to aging of the particles[14,15] and is not due to a quantum size effect.[7,9]

In the present paper, we present, for the first time, the magnetic properties of 4-nm Cd$_{1-y}$Mn$_y$S nanocrystals at various compositions. Furthermore, we attempt to relate the change in the optical properties to interactions involving manganese ions.

II. Experimental Techniques

II.1. Products. Sodium bis(ethyl-2-hexyl) sulfosuccinate, Na(AOT), was from Sigma and sodium sulfide (Na$_2$S) from Janssen. The solvents isooctane, isopentane, and methylcyclohexane were obtained from Fluka, ethanol from Prolabo, and heptane and dodecanethiol from Merck. Cadmium and manganese bis(ethyl-2-hexyl) sulfosuccinate [Cd(AOT)$_2$ and Mn-(AOT)$_2$] were synthesized in our laboratory as described previously.[16]

II.2. Apparatus. Optical absorption spectra were obtained with a Cary (1E) and HP 8452A UV−visible spectrophotometer.

Magnetic Properties of 4-nm Cd$_{1-y}$Mn$_y$S Nanoparticles

J. Phys. Chem. B, Vol. 103, No. 1, 1999 **5**

Photoluminescence spectra were recorded with a Spex fluorolog (1681).

An Oxford cryostat with a controller (ITC502) was used to control the sample temperature (77−300 K).

Energy dispersive spectrometry (EDS) measurements were made with a Link AN 10 000.

The EPR data were obtained using BRUKER ER 080 (200/60) spectrometers operating at 9.5 GHz (X-bands) for 103 < T < 298 K.

The measurements of magnetization (*M*) as functions of *H* and *T* were made using a SQUID magnetometer in the range −3 < *H* < 3 T and 3 < *T* < 10 K.

III. Magnetization and EPR Properties

III.1. Magnetization. Under a magnetic field, each spin of a Mn^{2+} ion inside the Cd$_{1-y}$Mn$_y$S nanoparticles contributes to the magnetic moment of the particle. An isolated Mn^{2+} ion, in a II−VI lattice, has a magnetic moment of $S = ^5/_2$ associated with the 3d^5 orbital.

When the composition of the manganese ions, *y*, is smaller than 0.001, the Mn^{2+} spins can be considered to be isolated. The magnetization, *M*, is described by the Brillouin function:

$$M = yN_0g\mu_BSB_S(g\mu_BSH/k_BT) \tag{1}$$

where N_0, B_S, H, and μ_B are the number of cations per unit of volume, the standard Brillouin function, the applied field, and the Bohr magneton, respectively, with $g = 2.0023$.

Above $y = 0.001$, due to Mn−Mn interactions, the standard Brillouin function cannot be applied and Gaj et al.[17] proposed an empirical expression to describe magnetization using the effective *T* and *S* parameters:

$$M = yN_0g\mu_BS_{eff}B_S(g\mu_BSH/k_BT_{eff}) \tag{2}$$

The S_{eff} values are always smaller than $^5/_2$. This is due to antiferromagnetic Mn^{2+} interactions that reduce magnetization and allow spin pair formation with a zero total magnetization.

The magnetic susceptibility, $\chi(y)$, measured at various compositions follows, at 77 K, a Curie−Weiss law:

$$\chi(T,y) = C_0y/[T + \Theta_0y] \tag{3}$$

where C_0y and Θ_0y are the Cd$_{1-y}$Mn$_y$S Curie constant and Curie temperature, respectively.

The Θ_0 and C_0 values are given by[8]

$$C_0 = N_0(g\mu_B)^2S(S + 1)/(3k_B) \qquad \Theta_0 = -(^2/_3)S(S + 1)ZJ/k_B \tag{4}$$

where N_0, Z, and J are the number of cations per unit volume (in the first approximation, N_0 does not depend on *y* in the range $0 < y < 0.3$), the number of nearest neighbors ($Z = 12$ for zinc-−blende DMS), and the nearest-neighbor exchange integral, respectively.[8] The Θ_0 and C_0 values are 409 K and 0.03 emu·g·K^{-1}, respectively. Taking into account the two constants, the variation of the susceptibility with composition was calculated, in the bulk phase, at 77 K from eq 3 (Figure 1A).

III.2. EPR Properties of DMS Bulk Materials. It is well-known that in a bulk DMS, with a low manganese ion concentration ($y < 0.001$), the hyperfine structure of the Mn^{2+} ions in tetrahedral sites (nuclear moment $I = ^5/_2$) is observed.[18,19] This structure consists of six intense lines, corresponding to the allowed hyperfine transition ($\Delta m_I = 0$) between the Zeeman
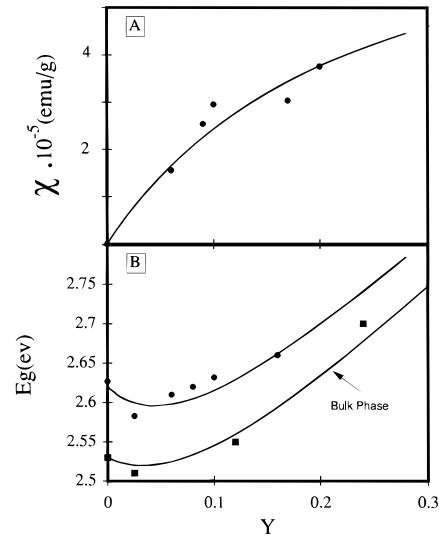

Figure 1. (A) Calculated (−) and (●) measured, at 77 K, magnetic susceptibility variation with composition. (B) Variation of the energy band gap with composition at 77 K for nanoparticles (●) and at 114 K for the bulk phase (■). (−) Calculated data.

sublevels ($m_S = \pm^1/_2$). The weaker lines observed between each principal line correspond to forbidden transitions ($\Delta m_I = \pm1$).[19]

In bulk DMS materials,[6,20−22] increasing *y* causes a rapid broadening of the hyperfine structure until a single line is observed. At higher compositions ($y > 0.001$), the EPR line width, ΔH_{pp}, markedly broadens with increasing *y*. Furthermore, for a given composition, ΔH_{pp} increases with decreasing temperature and $(\Delta H_{pp})_\infty$ can be deduced by extrapolation of the plot of ΔH_{pp} versus $1/T$ to zero. The variation of $(\Delta H_{pp})_\infty$ with *y* is related to the magnetic interaction for which two models have been developed:[6]

(i) First, the interactions are treated as dipolar, leading to

$$\Delta H_\infty = \frac{22}{\gamma}\left[\frac{\gamma^4h^2}{r^6}\right]\frac{h}{J}\frac{y}{\sqrt{y + 0.07}} \tag{5}$$

where *r* is the nearest Mn^{2+}−Mn^{2+} neighbor distance.

(ii) Second, the Dzyaloshinski−Moriya theory (D−M)[23] assumes that the anisotropic interactions, with a $(\Delta H_{pp})_\infty$ value depending on composition, are as follows:

$$\Delta H_\infty = \frac{10.5}{\gamma}\left(\frac{\lambda}{u}\right)^2\frac{J}{h}\frac{y}{\sqrt{y + 0.1}} \tag{6}$$

where *J*, γ, λ, and *U* are the nearest-neighbor Mn^{2+}−Mn^{2+} exchange constant (for bulk Cd$_{1-y}$Mn$_y$S, $J = 10.6$ K), the gyromagnetic ratio, the relevant spin−orbit coupling constant in the D−M treatment, and an effective energy scale that enters into the superexchange mechanism ($\lambda = 0.025$ eV and $U = 6$ eV), respectively.

The isotropic superexchange interactions are correlated to the Mn 3d states hybridized with semiconducting s- and p-derived levels; for Cd$_{1-y}$Mn$_y$Te and Cd$_{1-y}$Mn$_y$Se, they are dominant and couple the Mn spins antiferromagnetically, which explains the EPR line broadening.[1,5,6] By contrast, this model does not account for the Cd$_{1-y}$Mn$_y$S bulk material.[1,6]

IV. Synthesis and Optical Properties of 4-nm Cd$_{1-y}$Mn$_y$S Nanosized Particles Differing by Their Compositions

Syntheses of diluted magnetic semiconductors are performed in reverse micelles. A coprecipitation takes place by mixing

TABLE 1: Relative Concentration Used for Synthesis (y_s) Compared to Nanoparticle Manganese Concentration Measured by EDS (y)

y_s	0.01	0.05	0.2	0.3	0.4
y	0.006^a	0.03	0.1	0.17	0.2

a Estimated concentration.

two micellar solutions having the same water content, $w = $ [H$_2$O]/[AOT] = 40: One is made of 0.1 M Na(AOT) containing S^{2-} ions. The other one is a mixed micellar solution made of Cd(AOT)$_2$, Mn(AOT)$_2$, and Na(AOT)

The relative amount of Mn(AOT)$_2$ compared to Cd(AOT)$_2$ is defined as $y_S = $ [Mn(AOT)$_2$]/([Cd(AOT)$_2$] + [Mn(AOT)$_2$]). The concentration of cation ([Cd^{2+}] + [Mn^{2+}]) used for the syntheses is equal to 2.5×10^{-4} M.

Syntheses are performed at various ratios of Mn(AOT)$_2$ and Cd(AOT)$_2$ and in the presence of an excess of sulfur ions. The ratio $x = $ ([Cd^{2+}] + [Mn^{2+}])/[S^{2-}] is kept constant and equal to $^1/_2$.

At the end of the reaction, dodecanethiol is added to the micellar solution containing the crystallites (2 μL per mL of solution). A selective surface reaction occurs between the thio derivative and the cadmium and manganese ions at the interface. The nanocrystallites are kept 48 h in micellar solution. Then the solvent is removed by evaporation. This allows extraction of the particles from the micellar solution. The coated particles are washed three times with ethanol to remove surfactant and dispersed in a mixture of two solvents (isopentane−methylcyclohexane, 3 v/v) forming an optically clear glass at low temperatures.

Hence, syntheses have been performed at fixed water contents, $w = $ [H$_2$O]/[AOT] = 40, that is to say, at fixed droplet sizes and various y_S.

The coated particles synthesized in reverse micelles are extracted from the colloidal solution and analyzed by energy dispersion spectroscopy, EDS,[25] and the composition of Cd$_{1-y}$Mn$_y$S is measured. y was determined by averaging data taken from several different areas of the sample grid. Table 1 shows the EDS results of nanoparticles obtained for different reactant concentrations (Cd(AOT)$_2$ and Mn(AOT)$_2$). It shows that only a small amount of manganese remains in the CdS matrix. This is confirmed by the fact the absorption spectrum of the filtrate obtained by washing the coated particles is similar to that obtained for MnS particles.

For $y > 0.17$, inhomogeneities in composition are observed. The polydispersity was evaluated to 25%.

For $y = 0.006$, the sensitivity of the EDS technique is not high enough to detect such low amounts of manganese in the CdS matrix. This value has been extrapolated from the various experimental conditions in which the EDS technique is valid.

The average sizes of the coated particles and the standard deviation are determined by TEM[24] and from a histogram plot of about 500 particles, respectively. The average diameter of particles is 4 nm with a standard deviation of 11%.

The nanocrystal structure, determined from electron diffraction, is zinc blende, whereas it is wurtzite in the bulk phase. This confirms previous data obtained with II−VI semiconductor nanoclusters.[26,27] No diffractograms corresponding to MnS or MnO were observed.

V. Results

V.1. Changes in the Band Gap and the Fluorescence Yield Due to Isolated Manganese of 4-nm Cd$_{1-y}$Mn$_y$S as a Function of Composition. For a fixed composition, a red shift

in the absorption spectrum with increasing particle size occurs. The direct band-gap energy, deduced from the absorption spectrum,[28] increases with decreasing the particle size. This is a direct result of the quantum confinement effects.[29,30]

For a given average particle size, the band gap does not vary monotonically with composition and a minimum is observed at around 5%. This was obtained at 77 K (Figure 1B) and at room temperature.[14] Similar behaviors were observed in the bulk phase at 114 K.[31] The appearance of the minimum in the energy band gap with increasing composition cannot be attributed to a chemical disorder as described, for the bulk phase, by[31]

$$Eg(y,T) = Eg(CdS) + \Delta Ey - cy(1 - y) \qquad (7)$$

where Eg(CdS) and ΔE are the band-edge energy without Mn^{2+} and the variation of band-gap energy between CdS and MnS (assuming a linear relationship), respectively. The parameter c is the chemical disorder constant. The simulated band gap deduced from various c values never fits the experimental data.

In the bulk phase,[31] the minimum of the band-gap energy is induced by exchange interactions of the conduction and valence band electrons with the Mn^{2+} d electrons. The energy band gap is related to temperature and susceptibility by[33]

$$Eg(y,T) = Eg(CdS) - AT^2/(T + B) + \Delta Ey - b\chi(y)T \quad (8)$$

where $\chi(y)$ and T are the susceptibility of the material and the temperature, respectively. A, B, and b are constants. The first two parameters (A and B) depend on the material, whereas the last one (b) takes into account the exchange interactions between the Mn^{2+} d electrons and the band electrons. The A and B values are determined from the variation of the energy band gap, at a given composition, with temperature. They are size independent and equal to $(5.6 \pm 0.7) \times 10^{-4}$ eV·K^{-1} and 256 $\pm$ 14 K, respectively.

At 77 K, $\chi(y)$ is measured at various y. A rather good agreement between the experimental data obtained for 4-nm particles and the calculated susceptibility curve for the bulk phase is obtained, (Figure 1A). This permits a determination at 77 K of the b factor deduced from the best fit between the variation of the band-gap energy with composition via eq 8. The best fit between the experiment and simulation is obtained for b equal to 125 eV·g·Oe·emu^{-1}·K^{-1}. This value is higher than that deduced from the same fit taking into account data published for the bulk phase[31] (88 eV·g·Oe·emu^{-1}·K^{-1}). This indicates an increase in the exchange interactions between the Mn^{2+} d electrons and the band electrons.

The photoluminescence spectrum of Cd$_{0.95}$Mn$_{0.05}$S nanocrystals, recorded at 77 K ($\lambda_{ex} = 400$ nm), shows an emission due to CdS defect states around 700 nm and a band centered at 585 nm. The spectrum is fitted by assuming that two Gaussian curves and two spectra are derived: The spectrum designated 1 in Figure 2 is characterized by a maximum centered at 585 nm and attributed to the isolated Mn^{2+} in tetrahedral coordination.[34] The simulated half-width of the Mn^{2+} luminescence is 0.23 eV, which is in good agreement to that determined for Mn^{2+} luminescence in the bulk phase[34] and in Zn$_{1-y}$Mn$_y$S nanoclusters.[7,9,10,35] The relative ratio of 585-nm and 700-nm PL intensities increases with increasing y to reach a maximum at 0.08 (Figure 3A). This is attributed to an increase in the number of isolated ions in the CdS matrix. The 0.08 composition corresponds to the maximum of isolated Mn^{2+} states.

V.2. Magnetic Measurements. The magnetization curves recorded at 3 and 10 K and various compositions ($0.006 < y < $
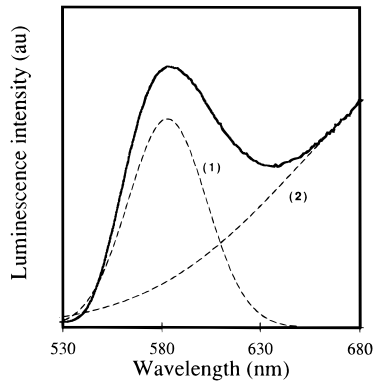
Magnetic Properties of 4-nm $Cd_{1-y}Mn_yS$ Nanoparticles

J. Phys. Chem. B, Vol. 103, No. 1, 1999 **7**

Figure 2. (A) Photoluminescence spectrum of 4-nm $Cd_{0.95}Mn_{0.05}S$ nanoparticles, recorded at 77 K. 1 and 2 are simulated curves assuming two Gaussians.

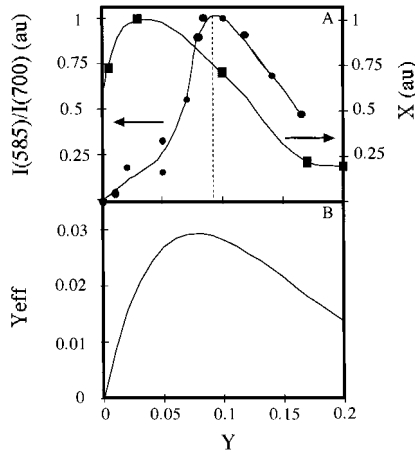**TABLE 2: S_{eff} and T_{eff} Values of Nanoparticles, as Well as the Fitting Parameters Deduced from Magnetization Curves**

| | 4-nm $Cd_{1-y}Mn_yS$ | | | | $S_{eff}{}^a$ for bulk $Cd_{1-y}Mn_yS$ | | |
| | 3 K | | 10 K | | | | |
y	S_{eff}	T_{eff}	S_{eff}	T_{eff}	1.5 K	5.7 K	10.9 K
0.006	1.76	4.7					
0.03	0.78	3.5	0.87	10	1.53^a		
0.1	0.54	5	0.63	10	0.95^a		
0.15^a					0.79^a	0.81^a	0.85^a
0.17	0.48	4.7	0.53	10			
0.2	0.38	4.6	0.47	10	0.37^a		

[a] Obtained on the bulk material by Chen et al.[40]

Figure 3. (A) Relative variation of 4-nm $Cd_{1-y}Mn_yS$ nanoparticles of the ratio of emission intensities I_{585}/I_{700} and on X with composition. (B) Variation of y_{eff} with y.

0.2) are in good agreement with the calculated curves obtained by using the modified Brillouin function (Figure 4).

Table 2 shows a decrease in the S_{eff} values with increasing y and with decreasing temperature. This is due to antiferromagnetic Mn^{2+} interactions that reduce magnetization and can reach

pair formation with a zero total magnetization. The S_{eff} values deduced for various compositions of 4-nm $Cd_{1-y}Mn_yS$ nanocrystals are always smaller than $^5/_2$ and larger than those determined for the bulk $Cd_{1-y}Mn_yS$ (Table 2). This indicates an increase in the interactions for 4-nm $Cd_{1-y}Mn_yS$ nanocrystals compared to the bulk phase.

The effective temperature, T_{eff}, is equal to the experimental one, at 10 K, whereas it is higher at 3 K (Table 2). The positive value of T_{eff} reflects antiferromagnetic interactions between Mn^{2+} ions.

V.3. EPR Spectroscopy of 4-nm $Cd_{1-y}Mn_yS$ Differing by Their Compositions. Figure 5 shows the EPR spectra of 4-nm $Cd_{1-y}Mn_yS$ nanocrystals recorded at various compositions (0.006 < y < 0.2) at room temperature. Each spectrum is made up of two parts:

(i) The first is a hyperfine structure with six lines existing on each spectrum. By increasing the manganese composition, the intensity of these peaks decreases and disappears, at y = 0.2.

(ii) The second is a broad, observed spectrum due to $Mn-Mn$ interactions. This spectrum can be fitted by a Lorentzian curve, and the peak-to-peak line width, ΔH_{pp}, is deduced. The ΔH_{pp} value is deduced for various y (Table 3). The y increase leads to the broadening of the EPR line.

From the difference between the experimental spectrum and that obtained from the Lorentzian curve, a hyperfine structure was deduced that is characteristic of isolated Mn^{2+} ions in a tetrahedric site with a nuclear hyperfine splitting of 69 G.
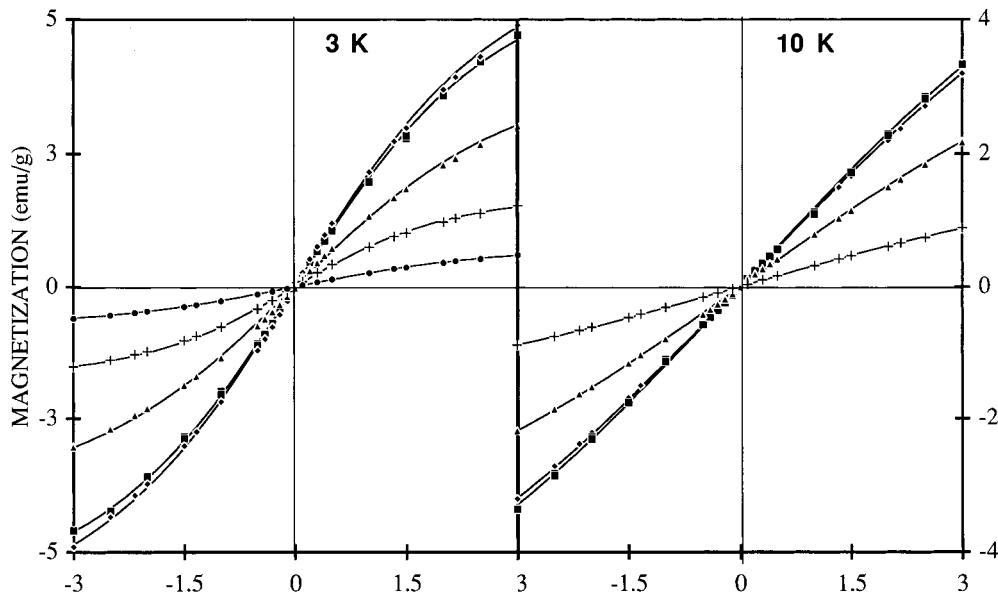

Figure 4. Magnetization curves of 4-nm $Cd_{1-y}Mn_yS$ nanoparticles, recorded at 3 and 10 K, over the compositions 0.006 < y < 0.2. The solid lines are the modified Brillouin function simulations. (■) y = 0.2, (◆) 0.17, (▲) 0.1, (+) 0.03, (●) 0.006.

Feltin et al.

TABLE 3: Peak-to Peak Line Widths (ΔH_{pp} (G)) Obtained after Subtracting a Lorentzian Fit from the Experimental Spectra for Compositions $0.006 < y < 0.2$ at $103 < T < 298$ K

	ΔH_{pp}								
y	100 K	103 K	120 K	130 K	150 K	200 K	250 K	298 K	$(\Delta H_{pp})_\infty$
0.006		135			115	105	95	90	68
0.03		195			175	160	149	144	118
0.1		225			205	190	185	180	156
0.2		270			245	230	220	215	186
0.25[b]	120[b]		115[b]	112[b]	110[b]				
0.33[b]	225[b]			208[b]	190[b]	160[b]			40[b]

[a] Determined by extrapolation as shown in Figure 9. [b] Obtained by Samarth and Furdyna.[6]

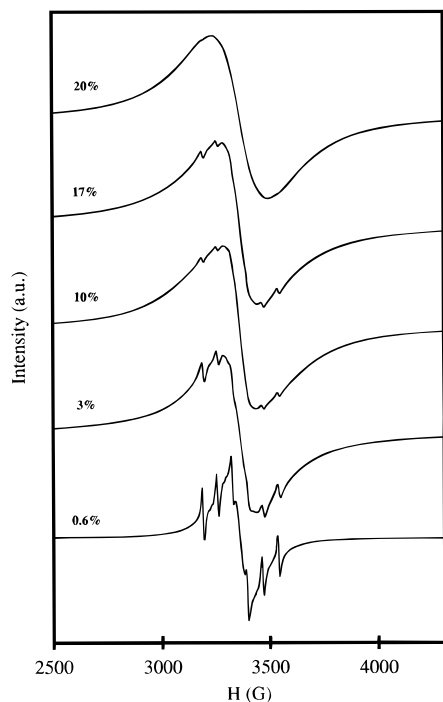**Figure 5.** EPR spectra of 4-nm Cd$_{1-y}$Mn$_y$S nanoparticles recorded at the compositions $0.006 < y < 0.2$, with a microwave frequency $\nu = 9.43$ GHz, at room temperature and $P = 10.2$ mW.

Figure 6. EPR spectra of 4-nm Cd$_{99.004}$Mn$_{0.006}$S nanoparticles recorded at various temperatures with a microwave frequency $\nu = 9.43$ GHz and $P = 10.2$ mW.

Figure 7. EPR spectrum of the hyperfine structure recorded at 103 K using a microwave frequency of $\nu = 9.43$ GHz and $P = 10.2$ mW.

The EPR spectra were recorded at various temperatures for $y = 0.006$. Upon decreasing the temperature, Figure 6 shows an increase in the broading of the Lorentzian subspectrum and a more defined hyperfine structure. At 103 K, the hyperfine structure deduced from the difference between the experimental spectrum and the Lorentzian fit shows six well-defined intensive lines and, between each of them, two weaker lines corresponding to a forbidden transition (Figure 7).

The EPR spectrum was recorded at various temperatures ($103 < T < 298$ K) and compositions ($0.006 < y < 0.33$). The ΔH_{pp}'s, were deduced from the Lorentizan fit of the broadest spectrum and were seen to increase with decreasing temperature on increasing composition.

The integral of the hyperfine structure and the Lorentzial curve have been calculated from the experimental data given in Figure 5. The ratio, X, of these integrals was determined at various compositions and was seen to increase with increasing composition, reaching a maximum around $y = 0.05$. Figure 3A shows that the variation with composition of X and the relative fluorescence due to isolated Mn^{2+} follow the same behavior. The relatively isolated Mn^{2+} ions in the CdS matrix on the nanoscale range increase with increasing composition, reaching a maximum at $y = 0.08$. The fluorescence technique is more sensitive than EPR and permits us to claim that the maximum is reached at $y = 0.0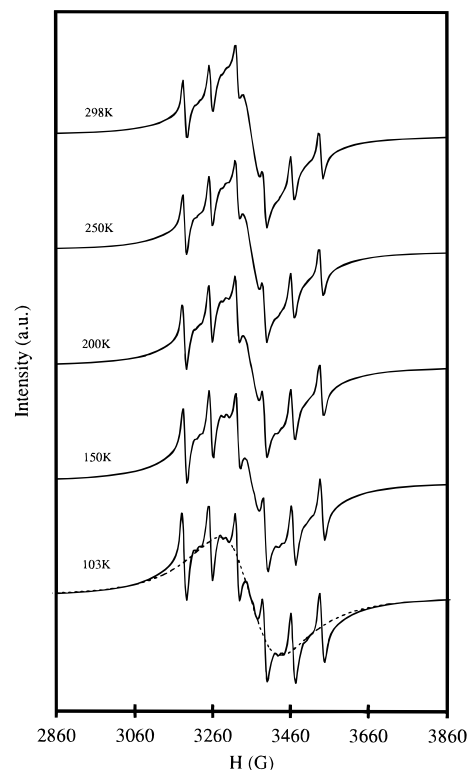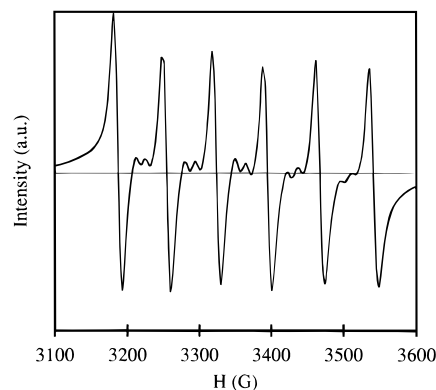8$. This can be correlated to the calculated number of isolated Mn^{2+} in the CdS matrix, y_{eff}, with composition,[36] (Figure 3B), which is characterized by a maximum around 0.1. These experimental data confirm those obtained in the bulk phase, which indicate that the fluorescence centered at 585 nm is due to isolated Mn^{2+} in the tetrahedral coordination. However, compared to the bulk phase, the
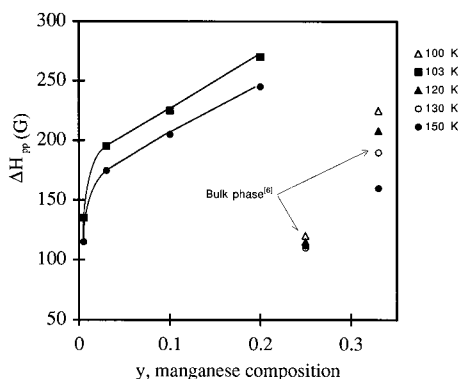
Magnetic Properties of 4-nm $Cd_{1-y}Mn_yS$ Nanoparticles

J. Phys. Chem. B, Vol. 103, No. 1, 1999 **9**

Figure 8. Variation of the peak-to-peak line width (ΔH_{pp}) with composition.
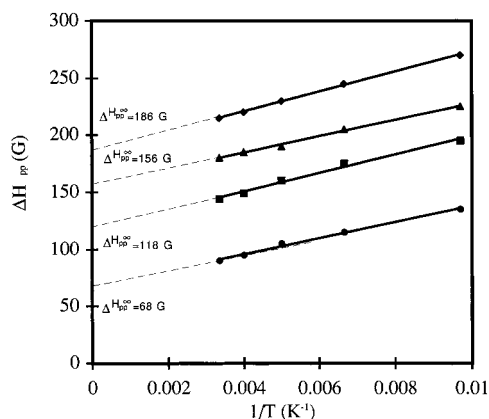

Figure 9. Variation of the peak-to-peak line width (ΔH_{pp}) with temperature at various manganese compositions, $y = 0.2$ (◆), 0.1 (▲), 0.03 (■), 0.006 (●).
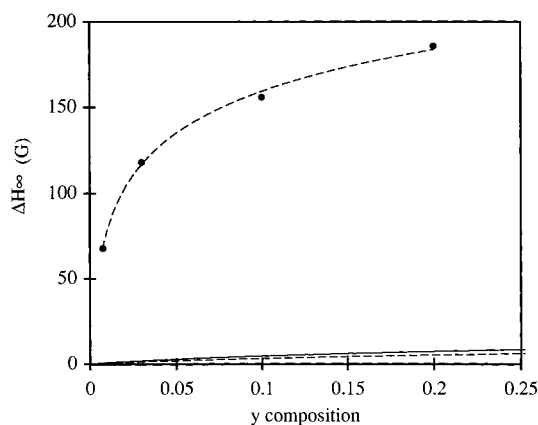

Figure 10. Variation of (ΔH_{pp})$_\infty$ with the composition of the 4-nm $Cd_{1-y}Mn_yS$ nanoparticles and for the bulk phase obtained by Samarth and Furdyna.[6]

fluorescence due to isolated Mn^{2+} in the tetrahedral site is observed for a higher composition ($y = 0.08$) rather than the range of $0.01 < y < 0.02$.[37-39]

Whatever the temperature, the ΔH_{pp} values were markedly higher that those obtained for the bulk phase[6] (Figure 8), indicating an increase in the Mn−Mn interactions.

Figure 9 shows that, for various y values, a linear ΔH_{pp} decreases with increasing $1/T$. This behavior is similar to that obtained for the DMS bulk phase,[6,21,22] where the susceptibility followed, at high temperature, a Curie−Weiss law expressed as

$$\Delta H_{pp} = (\Delta H_{pp})_\infty (1 + \Theta/T) \qquad (9)$$

where Θ and (ΔH_{pp})$_\infty$ are the Curie−Weiss temperature and the zero extrapolation of the plot of ΔH_{pp} versus $1/T$, respectively. In the bulk phase,[6] a similar plot (ΔH_{pp} versus $1/T$) was obtained for $Cd_{1-y}Mn_yS$, $Cd_{1-y}Mn_ySe$, and $Cd_{1-y}Mn_yTe$. For $Cd_{1-y}Mn_yS$, at $y = 0.33$, Samarth et al.[6] found a (ΔH_{pp})$_\infty$ value of 40 G, which was far below the (ΔH_{pp})$_\infty$ values obtained for 4-nm nanoparticles (Table 3).

Figure 10 compares, at various compositions, the increase of (ΔH_{pp})$_\infty$ with the models described above. No correlation was found between the models and the experiments. Similar conclusions can be made for the bulk phase for which neither model could fit the variation of (ΔH_{pp})$_\infty$ in the $Cd_{1-y}Mn_yS$ bulk phase.[6] However, a good correlation between the exchange interaction model and the experimental data was obtained for $Cd_{1-y}Mn_ySe$ and $Cd_{1-y}Mn_yTe$ bulk phase as shown in Figure 10.

VI. Discussion

The two parameters, S_{eff} and T_{eff}, deduced from the modified Brillouin function (eq 2) take into account the effect of the antiferomagnetic clustering.

S_{eff} is the effective mean spin of the Mn^{2+} ions ($S_{eff} < 5/2$). It decreases with increasing Mn^{2+} composition since the probability of magnetic ions occupying neighboring lattice sites increases. S_{eff} also inversely proportional to the strength of interactions. At a given composition, Table 2 shows that the S_{eff} values deduced for the $Cd_{1-y}Mn_yS$ bulk phase are higher than those observed for the nanoparticles. This indicates that the number of spin-correlated antiferromagnetic clusters is higher in the nanoparticles. This is due to stronger interactions in nanomaterials compared to the bulk phase.

The EPR experiments showed an increase in the line width with increasing composition. This further indicates an increase in the Mn−Mn interactions with increasing composition. Comparing the ΔH_{pp} values at various temperatures, for the nanocrystals and the bulk phase, Figure 8 clearly shows an increase in the ΔH_{pp} value for nanocrystals. Similar behavior is observed on the variation of (ΔH_{pp})$_\infty$ with composition. This is consistent, for a given composition, with the marked decrease of the S_{eff} value observed in nanocrystals compared to the bulk phase. From these data, it can be concluded that Mn−Mn interactions markedly increase in nanocrystal range compared to the bulk phase. These data can be related to the increase in the b factor obtained from the simulated curve. According to eq 8, the b factor takes into account the exchange interactions between Mn^{2+} ion d electrons and the band electrons. From this, it can be concluded that in the nanoscale range, the exchange interactions involving Mn^{2+} ions and exciton increase.

The good correlation between the EPR hyperfine structure and the fluorescence centered at 585 nm shown in Figure 3A clearly confirms that the fluorescence is due to isolated manganese ions in a tetrahedral coordination, as in the bulk phase. However, some differences in the nanoscale range compared to the bulk phase are observed: The fluorescence due to isolated Mn^{2+} ions in tetrahedral coordination is observed in the bulk phase at very low compositions ($y < 0.001$). By increasing the Mn^{2+} content, the fluorescence disappears due to an increase in the manganese interactions.[14] By contrast, in the nanoscale range, the amount of isolated Mn^{2+} increases with composition to reach a maximum around $y = 0.08$.

The superexchange model does not account the experimentally determined (ΔH_{pp})$_\infty$ values obtained at various compositions for the nanoparticles. Similarly the model does not fit data measured for the $Cd_{1-y}Mn_yS$ bulk phase.[6]

T_{eff} is an effective antiferromagnetic temperature ($T_{eff} > T_{real}$) and may increase with increasing y. The evolution of this later parameter is not so clear.

VII. Conclusion

For the first time, we demonstrate that the magnetic properties of 4-nm $Cd_{1-y}Mn_yS$ nanocrystals are markedly enhanced compared to those observed in the bulk phase. The variation with composition, y, of the luminescence and the EPR hyperfine structure, due to isolated Mn^{2+} in the tetrahedral site, presents similar behavior. The behavior markedly differs in the bulk phase and in the nanoparticles: The fluorescence due to isolated Mn^{2+} ions is observed at a rather large composition in the nanoparticles compared to the bulk phase. The exchange interaction of the band electrons with the Mn^{2+} seems to be correlated to the $Mn^{2+}-Mn^{2+}$ interactions.

References and Notes

(1) Furdyna, J. K.; Kossut J. *Semiconductors and semimetals*; Academic: New York, 1988; Vol. 25.

(2) Gaj, J. A. Proc. 15th Internat. Conf. Physics of semiconductors. *J. Phys. Soc. Jpn.* **1980**, *49*, suppl. A, 797.

(3) Bastard, G.; Rigaux, C.; Mycielski, A. *Phys. Status Solidi B* **1977**, *79*, 585.

(4) Dietl, T.; Spalek, *J. Phys. Rev. Lett.* **1982**, *48*, 355.

(5) Larson, B. E.; Hass, K. C.; Ehrenreich, H.; Carbson, A. E. *Phys. Rev. B* **1988**, *37*, 4137.

(6) Samarth, N.; Furdyna, J. K. *Phys. Rev. B* **1988**, *37*, 9227.

(7) Bhargava, R. N. *J. Lumin.* **1996**, *70*, 85.

(8) Furdyna, J. K. *J. Appl. Phys.* **1988**, *64*, R29.

(9) Bhargava, R. N.; Gallagher, D.; Hong, X.; Nurmikko, A. *Phys. Rev. Lett.* **1994**, *72*, 416.

(10) Wang, Y.; Herron, N.; Bein, T. *Solid State Commun.* **1991**, *77*, 33.

(11) Oka, Y.; Yanata, K. *J. Lumin.* **1996**, *70*, 35.

(12) Biernachi, S.; Kutrowski, M.; Karczewski, G.; Wojtowicz, T.; Kossut, J. *Semicond. Sci. Technol.* **1996**, *11*, 48.

(13) Levy, L.; Hochepied, J. F.; Pileni, M. P. *J. Phys. Chem.* **1996**, *100*, 18332.

(14) Levy, L.; Feltin, N.; Ingert, D.; Pileni, M. P. *J. Phys. Chem.* **1997**, *101*, 9153.

(15) Levy, L.; Ingert, D.; Feltin, N.; Pileni, M. P. *Adv. Mater.* **1998**, *10*, 53.

(16) Petit, C.; Lixon, P.; Pileni, M. P. *Langmuir* **1991**, *7*, 2620.

(17) Gaj, J. A.; Planel, R.; Fishman, G. *Solid State Commun.* **1979**, *29*, 435.

(18) Dorain, P. B. *Phys. Rev.* **1958**, *112*, 1058.

(19) Misra, S. K. *Appl. Magn. Reson.* **1996**, *10*, 193.

(20) Aliev, M. N.; Tagirov, L. R.; Tagiev, V. S. *J. Magn. Reson. A* **1996**, *123*, 16.

(21) Oseroff, S. B. *Phys. Rev. B* **1982**, *25*, 6584.

(22) Sayad, H. A.; Bhagat, S. M. *Phys. Rev. B* **1985**, *31*, 591.

(23) Dzyaloshinsky, J. *J. Phys. Chem. Solids* **1958**, *4*, 241. Moriya, T. *Phys. Rev.* **1960**, *120*, 91.

(24) A JEOL (100-kV) Model JEM 100CX II was used for transmission electron microscopy (TEM) vand electron diffraction.

(25) Energy dispersive spectrometry (EDS) measurement was obtained by a Link AN 10 000.

(26) Cizeron, J.; Pileni, M. P. *J. Phys. Chem.* **1995**, *99*, 17410.

(27) Vogel, W.; Urban, J.; Kundu, M.; Kulkarni, S. K. *Langmuir* **1997**, *13*, 827.

(28) Wang, Y.; Herron, N. *J. Phys. Chem.* **1991**, *95*, 525.

(29) Brus, L. E. *J. Chem. Phys.* **1983**, *79*, 5566.

(30) Petit, C.; Pileni, M. P. *J. Phys. Chem.* **1988**, *92*, 2282.

(31) Ikeda, M.; Itoh, K.; Hisarro, S. *J. Phys. Soc. Jpn.* **1968**, *25*, 455.

(32) Thompson, A. G.; Wolley, J. C. *Can. J. Phys.* **1967**, *45*, 255.

(33) Bylsma, R. B.; Becker, W. M.; Kossut J.; Debska, U. *Phys. Rev. B* **1986**, *33*, 8207.

(34) Gumlich, H. E. *J. Lumin.* **1981**, *23*, 73.

(35) Bhargava, R. N.; Gallager, D.; Welker, T. *J. Lumin.* **1994**, *60&61*, 275.

(36) Kreitman, M. M.; Barnett, D. L. *J. Chem. Phys.* **1965**, *43*, 364.

(37) Katiyar, M.; Kitai, A. H. *J. Lumin.* **1990**, *46*, 227.

(38) Warren, A. J.; Thomas, C. B.; Reehal, H. S.; Stevens, P. R. C. *J. Lumin.* **1983**, *28*, 147.

(39) Yu, I.; Senna. M. *Appl. Phys. Lett.* **1995**, *66*, 424.

(40) Chen, C.-J.; Qu, M.; Hu, W.; Zhang, X.; Lin, F.; Hu, H.-B.; Ma, K.-J.; Giriat, W. *J. Appl. Phys.* **1991**, *69*, 6114.